Microporosity in aluminium foams

M. Mukherjee[1,2,*], F. García-Moreno[2], C. Jiménez[2], A. Rack[3], J. Banhart[2,4]

[1]Department of Metallurgical and Materials Engineering, Indian Institute of Technology Madras, Chennai 600036, India

[2]Helmholtz Centre Berlin, Hahn-Meitner-Platz 1, 14109 Berlin, Germany

[3]European Synchrotron Radiation Facility, 38043 Grenoble Cedex, France

[4]Technische Universität Berlin, Hardenbergstrasse 36, 10623 Berlin, Germany

Abstract

We studied microporosity in the metallic matrix of aluminium foams produced by the powder metallurgical route both with and without application of a blowing agent. Microporosity was studied in-situ in liquid metal foams as well as ex-situ in the solidified microstructure. In-situ studies were carried out using synchrotron X-rays. Quantitative analyses of the amount and distribution of microporosity inside cell walls, Plateau borders and nodes were performed on 2D micrographs and on 3D reconstructed volumes generated by X-ray tomography. We studied the influence of alloying elements, blowing agent and holding time on the amount and type of micropores. The mechanisms of microporosity formation and the evolution of microporosity via diffusion of hydrogen and by coalescence are discussed. It was observed that the alloy composition and holding time have a strong influence on microporosity. Different possible strategies to control microporosity are suggested.

Keywords: Metal foam; Solidification; Defects; Hydrogen Diffusion; Microporosity

---

*Corresponding author: manas.mukherjee@gmail.com

1. Introduction

Microporosity is inevitable in aluminium alloys [1-4]. The amount of microporosity is determined by the solidification conditions and alloying elements. While insufficient feeding during solidification leads to shrinkage microporosity, the difference in hydrogen solubility between liquid and solid aluminium results in gas microporosity [2]. Microporosity adversely affects properties such as tensile strength [1, 4] and fatigue [3] because it promotes stress concentration. Foams made from aluminium alloys also contain such microporosity. We study it in this article.

At present, the disparity between the predicted and measured strength of aluminium foams is attributed to the presence of a non-uniform cell size distribution and defects such as missing or broken cell walls, elliptical cells and curvature in cell walls [5-7]. However, the effect of microporosity is not taken into account. It has been reported that castings of thin sections are more vulnerable to the effects of micropores because they reduce the load-bearing cross section considerably [1]. The same also applies to closed-cell metal foams, which are made of thin sections such as cell walls and Plateau borders, usually with thicknesses of 50–300 μm. This implies that the tensile and fatigue properties of closed-cell metal foams are also affected by microporosity.

The plastic collapse stress of foams scales with the relative density of foams as follows [8]:

$$\frac{\sigma_{pl}^{*}}{\sigma_{YS}} = 0.3\left(\phi\frac{\rho^{*}}{\rho_s}\right)^{3/2} + 0.4(1-\phi)\frac{\rho^{*}}{\rho_s} \qquad (1)$$

where ρ^{*} and σ_{pl}^{*} are the density and plastic collapse stress of the foam, ρ_s and σ_{YS} are those of the solid cell wall material. ϕ is the volume fraction of solid contained in the cell edges and the

remaining fraction (1-ϕ) is in the cell faces. In Eq. 1, the first term is for the bending of cell edges (Plateau borders) and the second term is for the stretching of cell faces (cell walls). A similar relationship that includes bending and stretching components also exists for Young's modulus. While stretching immediately implies tensile stresses, bending involves both tensile and compressive stresses. Indeed, it is shown from in-situ compression tests of aluminium foams that even under compressive loading, tensile stress is generated [9].Therefore, beside under tensile and fatigue loading, metal foams are expected to be susceptible to the effects of microporosity under compressive loading as well. While ρ^* in Eq. (1) takes into account the total porosity of the foam it does not provide any clue about the amount of microporosity. For example, a foam with $\rho^* = 0.18$ has 82% porosity and 18% solid fraction. Let us assume that out of this 82% porosity 2% is present in the form of microporosity in the microstructure of the solid part and the remaining 80% porosity is constituted by the volume of the cells. This suggests that the microstructure of the cell walls, Plateau borders and nodes contains 10% microporosity. While the influence of 2% porosity on the mechanical properties of a foam is marginal, the effect of 10% microporosity on the tensile strength of the metallic constituent cannot be ignored [10]. This implies that the relative density alone cannot predict the mechanical properties of a foam and the effect of microporosity should also be considered.

Ohgaki et al. [11] and Toda et al. [9, 12]were the first to draw attention towards the effect of microporosity in aluminium foams. A high level of microporosity (26%) was reported [11]. It was shown that in metal foams subjected to compressive stress cracks originate from micropores with diameter between 30 and 350 µm. This is because large strains accumulate at such micropores and therefore the borders of them might be crack initiation sites [11]. Our own

previous study has also shown that under compression of foams cracks are generated at micropores of deformed cell walls [13].

The goal of the present work is to quantify the amount and type of microporosity in aluminium alloy foams and clarify the mechanisms of microporosity formation. We also propose strategies to modify them in section 4.6.

2. Experimental

2.1. Materials

Aluminium (Alpoco, 99.7% pure, D_{50} = 38 µm), silicon (Wacker Chemie, 99.5% pure, D_{50} = 26 µm), copper (Chempur, 99.5% pure, D_{50} = 27 µm), pre-alloyed AlMg50 (Possehl Erzkontor GmbH, purity not specified) and TiH_2 serving as blowing agent (Chemetall, Grade N, 98.8% pure, D_{50} = 14 µm) powders were used to prepare foamable precursors. The TiH_2 was heat-treated at 480 °C for 180 min in air. To prepare the precursors, 30 g of metal powder were mixed with or without 0.5 wt.% of TiH_2 powder in a tumbling mixer for 15 min. The powder blend was subjected to uni-axial compaction in a cylindrical die at 400 °C for 5 min applying a pressure of 300 MPa. Four alloys were prepared with TiH_2 and two alloys were prepared without TiH_2 as specified in Table 1. Alloy AlSi6Cu4, was prepared both with and without TiH_2. Unless otherwise indicated, the version containing TiH_2 is meant. AlCu13Mg4 was prepared only without TiH_2. Cylindrical tablets (36 mm diameter, ~11 mm thickness) were obtained by uni-axial compaction. 10×10×4 mm^3 large samples were cut out from these tablets for foaming, ensuring that the compaction direction was along the 4-mm long side of the sample.

2.2. Foaming procedures

Two different furnaces were used for foaming. All samples containing TiH_2 were foamed inside a steel mould in air using a *lamp furnace* equipped with two or three halogen lamps of 150 W power [14], see also Ref. [15]. The temperature was measured at the bottom surface of the sample. TiH_2-free samples were foamed by gas pressure manipulation in a gas-tight *pressure furnace* equipped with a ceramic heating. The temperature was measured at the bottom surface of the sample and calibrated to extract the temperature of the foam interior (given in Table 1), see Ref. [15].

TiH_2-containing samples were foamed by heating them to above their melting point with a heating rate of 2–3 K/s. After the temperature had reached the foaming temperature it remained at or slightly above that level for a period which is denoted as *holding time* (HT). After holding, the foam was solidified by ambient cooling at an average cooling rate of about 1 K/s. To foam TiH_2-free samples, the powder compacts were first heated up to the foaming temperature inside the pressure furnace filled with argon at 5 bar pressure. After melting of the samples, the gas pressure was released to ambient pressure (1 bar) within 30 s. The pressure drop immediately induced expansion of the sample by the release and expansion of adsorbed gases present in the powder compact. This process is referred to as *pressure induced foaming* (PIF) [16-17]. After pressure release, the experimental course was identical to that of the samples containing blowing agent.

2.3. In-situ observation of foaming

Foaming of Al and AlSi6Cu4 was observed in-situ using hard X-ray synchrotron radiation at beamline ID19 of the European Synchrotron Radiation Facility. A mixed contrast mode of phase and absorption contrast was used for image acquisition where the contrast of the liquid-gas interfaces is dominated by refraction effects. The details of the experimental technique

are given in [18-19]. This configuration of the set-up ensured high visibility of the liquid-gas interface.

2.3. Structural characterization

The solidified foams were sectioned into two halves. One half was used for optical microscopy. The samples were embedded in cold-curing resin (Kulzer), mechanically ground using 120–4000 grit silicon carbide paper, polished successively with 3 and 1 μm diamond paste, and finally polished with a SiO_2 suspension on a smooth cloth. *ImageTool* version 3.00 software was used to analyse the microporosity from the 2D micrographs. From the other half of the AlSi6Cu4, AlSi6Cu4 without TiH_2 and AlCu13Mg4 alloy foams a small piece approximately $5\times5\times8$ mm^3 in size was excised for X-ray tomography. The details of the X-ray tomography is given in Ref. [13]. The software *MAVI* 1.3.1 was used for 3D quantitative analysis of micropores.

3. Results

3.1. Microstructure

Before introducing the results it is necessary to define the terms *micropores* and *microporosity*. Being a porous material, aluminium foam contains a wide range of pores and there is no sharp boundary between small and large pores. Following the observation of Ohgaki et al. [11], we label pores as micropores that have an equivalent diameter ≤350 μm. This is similar to the average size of the micropores (≈350 μm) observed in our own study [20]. In this article, the quantitative analysis presented (in Figs. 5 and 10) is based on pores with an equivalent diameter ≤350 μm. The total amount of micropores is referred to as microporosity. It is measured from the 2D micrographs of foam microstructure and defined as follows:

$$\text{microporosity} = \frac{\text{total area of micropores}}{\text{area of the solid matrix including micropores}}. \quad (2)$$

Accordingly, a certain level X of microporosity means that a fraction X of the area of the cell walls, Plateau borders and nodes is covered by micropores.

Figs. 1–4 show the microstructure (also macrostructure in Fig. 3) of all the foams. The microstructures reveal two types of microporosity – gas and shrinkage porosity. The former comes as circular void embedded in the cell wall material. The latter appears non-circular and as voids situated between former solid phase particles.

The microporosity of each sample was measured by analysing five to ten micrographs obtained from different parts of each sample. The result for all the alloys is plotted in Fig. 5. The microporosity in pure Al and AlSi11 foams is less than that in AlSi7 foams, which has 14% microporosity. Pure Al foams show only little, and AlSi7 and AlSi11 foams show no shrinkage microporosity, see Figs. 1a–1c, whereas the microstructure of AlSi7 foam reveals a significant amount of gas microporosity.

Fig. 2 shows how the microporosity in AlSi6Cu4 foam decreases with increasing HT (a to d). An enlarged view of a large and elongated micropores is shown in the inset of Fig. 2a. Here the micropore reveals the contour of dendrites, which is a signature of shrinkage porosity. Its large size implies that it also must contain some gas microporosity. Since shrinkage micropores grow in interdendritic channels, they appear as a network of irregular pores in the adjacent dendritic arms as marked in Fig. 2b. For 200 s HT, the 2D microporosity in the AlSi6Cu4 foam matrix is about 9%, which reduces to about 3% for 1500 s or longer HT as shown in Fig. 5. An identical trend was observed forAlSi6Cu4 foams without TiH_2. Microporosity decreases with HT as shown in Figs. 3a and 3b, about 9% for 200 s HT to about 3% for 1500 s HT. Unless otherwise specified, all the results and discussions for these two alloys

correspond to 200 s HT. The macrostructures of the AlSi6Cu4 foams without TiH_2in Figs. 3c and 3d reveal that while for 200 s HT there are many broken cell walls, the sample for 1500 s HT has only few of them. The AlCu13Mg4 foam matrix shows a large amount of microporosity, about 13%, which is mostly due to gas as evidenced by their circular shape in Fig. 4. No shrinkage microporosity was observed in this foam.

3.2. In-situ studies

Figs. 6 shows X-ray radioscopic images of AlSi6Cu4 foam in the liquid state. When a foam is liquid, a cell should be referred as bubble and a cell wall as film. Accordingly, a micropore in a liquid foam is referred to as microbubble. Plateau borders and nodes containing a large amount of melt are thicker than films. Microbubbles inside Plateau borders and nodes are of various sizes. Films contain only small microbubbles. It was observed that microbubbles coalesce with each other (see supplementary material A) as well as with bubbles of the foam as demonstrated in Fig. 6b and 6c.

Fig. 7a shows an X-ray radioscopic image of an Al foam in the liquid state in which several microbubbles can be seen. Six of them are marked by numbers. It was observed that microbubbles shrink with time. This was quantified by measuring the radius of these six microbubbles at 10 s interval for 40 s. The evolution of radius with time is given in Fig. 7c and shows that all microbubbles shrink with time but at a different rate. The zero value of radius for microbubble no.5 after 30 s indicates that this microbubble has disappeared after 30 s. The radiographs of all stages are provided in supplementary material B.

3.3. 3D distribution of pores

3D arrangements of micropores in AlSi6Cu4, AlSi6Cu4 without TiH_2 and AlCu13Mg4 foams are shown in Fig. 8. The micropores in the latter two foams are mostly spherical, whereas in

AlSi6Cu4 they are both spherical and elongated. Cell walls are seen as the thinner regions between two cells, while the thicker regions are either Plateau borders or nodes.

Fig. 9 reveals the 3D distribution of micropores embedded in the metallic matrix of AlSi6Cu4 foam. The micropores present in the nodes are the largest, while the ones in the cell walls are the smallest. The micropores in the Plateau borders are of intermediate size.

Fig. 10 compares the *shape factor* of the micropores in AlSi6Cu4, AlSi6Cu4 without TiH_2 and AlCu13Mg4 foams. For a micropore of volume V and surface area S the shape factor is defined as:

$$\text{Shape factor} = 6\sqrt{\pi}\,\frac{V}{\sqrt{S^3}} \qquad (3)$$

and takes values between 0 (non-spherical) and 1 (spherical). A strong difference in the shape factor of large micropores in these three alloys is noticeable. For example, if the micropores larger than 100 µm are compared, most of them in AlSi6Cu4 without TiH_2 and AlCu13Mg4 foams are near-spherical showing a peak around a shape factor of 0.9. On the contrary, in AlSi6Cu4 foam there are many large and elongated micropores.

4. Discussion

4.1. Shrinkage and gas microporosity

Irregular micropores are caused by solidification shrinkage, while hydrogen precipitation during solidification creates round micropores. However, any of the micropores can be caused by any or both of the mechanisms, since the morphology of a micropore is merely an indication of the predominant mechanism [2, 21].

In short-freezing range alloys such as pure metals and alloys with near-eutectic composition, feeding takes place freely until the last melt has solidified. As a result,

solidification shrinkage in these alloys is manifested as bulk shrinkage and not as microporosity. For long-freezing range alloys, feeding is inhibited as soon as the amount of solidified fraction becomes too high to allow for easy liquid flow. This leads to the formation of shrinkage porosity [2, 21]. AlSi6Cu4 alloy is a long-freezing range type (melting range 92 °C, see Table 2), which is the reason why shrinkage microporosity forms in AlSi6Cu4foams, see Fig.2. On the other hand, even though Al and AlSi11 have a similar amount of solidification shrinkage as the former alloy, they do not show any significant amount of shrinkage porosity because of their short-freezing range type, see Fig. 1a and 1c.

Because feeding is influenced by the solid fraction during solidification, it is necessary to estimate its amount in order to predict the level of difficulty in feeding. The equilibrium liquid fraction during solidification of AlSi7, AlSi6Cu4 and AlCu13Mg4 was calculated by the Calphad approach using the Thermo-Calc [22] software and the COST507 Gibbs energy database [23]and is displayed in Fig. 11. In the case of AlCu13Mg4 alloy, coming from the liquid state and reaching the eutectic temperature (503 °C), there is at least 25 wt.% eutectic liquid and 75 wt.% solid. This implies that feeding is not much restricted before the ternary reaction takes place. In contrast, for AlSi6Cu4 alloy the solid fraction exceeds 90 wt.% long before the eutectic reaction, see Fig. 11. Therefore, although AlCu13Mg4 is a long-freezing range alloy (melting range 101 °C, see Table 2), feeding in this alloy takes place without much resistance. At the eutectic temperature (577 °C) of AlSi7 alloy there is approximately 50 wt.% of eutectic liquid which facilitates feeding during the later stage of solidification. Hence, shrinkage microporosity does not form in AlSi7 and AlCu13Mg4 alloys.

Molten aluminium reacts with atmospheric moisture and produces hydrogen, a part of which dissolves in the melt. Decomposition of the blowing agent also provides hydrogen and is

an additional source of hydrogen in TiH_2 containing foams. During solidification, when the melt becomes saturated, this hydrogen is rejected from the solid phase at the solid-liquid interface. In the presence of nuclei such as oxide particles, already formed solid phase, etc., hydrogen micropores nucleate and grow and eventually get trapped as micropores in the solid phase [2, 21]. Microporosity formed from this gas consists of isolated micropores usually spherical in shape because they first appear as bubbles within the liquid.

Metal foams made of aluminium alloys invariably contain such shrinkage and gas microporosity. For a given solidification condition, the amount of microporosity depends on the alloy composition. Values for the solidification shrinkage and hydrogen solubility in the alloys used in this work are given in Table 2. The solubility values quoted in the literature refer to the volume at 300 K. When precipitated hydrogen forms micropores, one has to consider the effective volume at the precipitation temperature [15]. Based on this logic, hydrogen solubility at 700 °C was calculated using Wagner's interaction parameters [24-25] and are presented here as effective volume. Previously, we have estimated the amount of hydrogen precipitation at the liquidus temperature (T_L) of aluminium alloys [15]; this is also given in Table 2. Following the logic applied in Ref. [15] the hydrogen precipitation in AlCu13Mg4 alloy was estimated to about 3.8 vol.%.

Table 2 shows that hydrogen precipitation is the highest in pure Al, namely 5 vol.%. However, the amount of microporosity appearing mainly as gas microporosity in Al foam is less than 1%. Precipitated hydrogen diffuses to the surrounding atmosphere or to the cells while the foam is still in liquid state. The foaming temperature for Al foam was 670 °C, 50 K higher than that for the other alloys, which promotes faster diffusion of hydrogen compared to other alloy foams.

The values of solidification shrinkage presented in Table 2 were extracted from Refs. [2, 26-27]. The measured microporosity in AlSi6Cu4 is about 9% (Fig. 5). In contrast, according to the data in Table 2, the maximum possible microporosity due to the combined effect of solidification shrinkage and gas precipitation can be about 8.5%, which is slightly less than the maximum possible microporosity in this alloy. Solidification shrinkage does not produce microporosity in AlSi7, AlSi11 and AlCu13Mg4 alloys as discussed earlier. Therefore, microporosity in these alloys can only be created by hydrogen precipitation, which is about 3%, 2% and 4% (by volume), respectively, while the measured microporosity in these alloys is about 14%, 5% and 13%, respectively. These disparities point towards other sources of gas for micropores. Moreover, gas micropores were also observed in liquid foams held at constant temperature above the liquidus temperature of the alloy, see Figs. 6 and 7.

4.2. Other sources of gas for the formation of microporosity

Metal foams produced by the PM route contain two additional gas sources. One is the hydrogen that is produced by the decomposition of TiH_2. The second gas source is the gas generated by the decomposition of adsorbates that are present in metal powders either as hydroxides in the surface oxide layer [16-17] or as some other compound at the boundaries of the former metal powder particles [28]. The micropores shown in Figs. 6 and 7 are produced by either or both of these gas sources. AlSi6Cu4 foams produced without TiH_2 contain a similar amount of microporosity as AlSi6Cu4 foams produced with TiH_2. This suggests that adsorbates, which are common to both the foams, contribute a major part of this 9% microporosity in addition to shrinkage and gas microporosity.

4.3. Evolution of microporosity in liquid foam

The evolution of microbubbles in liquid foams follows the same patterns as that of large bubbles. Both are governed by coalescence and gas diffusion. The liquid film between two adjacent microbubbles (or bubbles) thins due to gravity and capillary drainage. At some point, mechanical perturbations rupture the film and lead to the coalescence of the two microbubbles (or bubbles) [29]. Either two smaller microbubbles coalesce forming a larger one (see supplementary material, Fig. S1) or a microbubble coalesces with a bubble as shown in Figs. 6b and 6c. While the former event does not change the amount of microporosity, the latter reduces it. Similarly, microporosity is reduced through diffusion only in the case where the gas of a microbubble diffuses into a bubble or to its surrounding.

The pressure inside a spherical microbubble is the sum of the metallostatic pressure, the atmospheric pressure (1 bar) and Δp, where Δp is the pressure exerted by surface tensional forces as derived from the Young-Laplace equation:

$$\Delta p = 2\gamma / r \quad (4)$$

Here, γ is the surface tension of the liquid and r is the radius of the microbubble. Although the surface tension of aluminium varies with oxygen content, alloying elements and temperature [30-31], we use γ of pure liquid aluminium, which at 660 °C is about 1 Nm^{-1} [32]. Accordingly, Δp for a spherical microbubble of radius 10 µm is 2 bar, whereas Δp for a spherical bubble of radius 1 mm is only 0.02 bar. The hydrogen concentration in each interface – from liquid Al to microbubble (Al-µB) or from liquid Al to a bubble (Al-B) – is in equilibrium with the respective pressure Δp. Sievert's law states that hydrogen solubility increases with the square root of pressure. Consequently, the solubility of hydrogen is higher at the Al-µB interface than at the Al-B interface.

Now we consider the diffusion of hydrogen from a μB of radius *r* to a bubble of radius *R* separated by a distance *d* as depicted in Fig.12. This sketch reflects the situation of a micropore as shown in Fig. 4. For simplicity, a few assumptions are made: The gas of a given μB diffuses only to the bubble. Since the entire surface of μB is not at a constant distance from the bubble, diffusion will be different from different parts of the μB. We consider that diffusion takes place only through the shaded region, which represents the shortest path for diffusion and in 3D covers 10% of the total surface area of the μB. The shaded region is assumed to be flat with a thickness *d*. If we consider a constant and linear concentration gradient between Al-μB and Al-B interfaces, then, according to Fick's first law, the diffusion rate from the μB to the bubble is given by the following equation [33]:

$$\frac{dV}{dt} = -D_{H\to Al} \times \frac{\Delta C}{d} \times A \times 0.1 . \qquad (5)$$

V is the volume of the μB, *A* its surface area, $D_{H\to Al}$ is the diffusion coefficient of hydrogen in liquid Al, namely 3.32×10^{-7} m^2 s^{-1} at 660 °C [34]. The negative sign in Eq. 5 implies that the volume of μB decreases with time. The factor 0.1 accounts for the 10% of *A*. The hydrogen concentration difference ΔC between the Al-μB and the Al-B interfaces can be estimated by applying Sievert's law to (for details see Appendix A):

$$\Delta C = \frac{S_H}{\sqrt{P_{\text{atm}}}}\left(\sqrt{P_{\text{atm}} + \frac{2\gamma}{r}} - \sqrt{P_{\text{atm}} + \frac{2\gamma}{R}}\right). \qquad (6)$$

The metallostatic pressure is negligible for such a small volume of foam in the current study and has therefore been ignored in the total pressure term. S_H is the solubility of hydrogen in liquid Al at atmospheric pressure ($P_{\text{atm}} = 10^5$ Pa) and the value of S_H at 660 °C is about 0.05 m^3/m^3 of Al

[33]. If from time $t = 0$ to time $t = t'$, the radius of the μB changes from r to r', and if $d << r$ then according to Ref. [33] Eq. 5 can be expressed as:

$$t' = \frac{(r - r') \cdot r \cdot d}{r' \cdot D_{H \to Al} \cdot \Delta C \cdot 0.1}. \quad (7)$$

Assuming realistic values R = 1 mm (= 10^{-3} m), r= 100 μm (= 10^{-4} m), d = 10 μm (= 10^{-5} m), then for 50% and 90% reduction in radius, t' is about 7.3 s and 66 s, respectively. If the radius of a μB decreases the pressure inside it increases resulting in a higher value of $C_{\text{Al-μB}}$. If we assume that d remains unchanged then the rate of gas diffusion increases further with decreasing r. This means that the shrinkage of the μB is accelerated with time, which was not considered in the model above. Nevertheless, it becomes evident that μBs in close contact with a bubble tend to disappear within a few seconds.

This can be verified by the results presented in Fig. 7c where all the microbubbles shrink to half of their size in 30 s to 40 s and μB no. 5 completely disappears after 30 s. It is not reasonable to compare these results directly with the estimation of gas loss through diffusion due to the following reasons. (a) The distance between a μB and a bubble cannot be derived from the X-ray projected images. (b) It is not clear whether during shrinkage of a μB its distance from a bubble remains constant or changes. (c) In the particular example of Fig. 7a, all the μBs are in the outer surface layer of the foam. Therefore, diffusion to the surrounding atmosphere can take place as well, in which case the rate of diffusion will be faster due to the larger pressure difference, resulting in a larger concentration gradient. (d) It is also possible that these μBs still receive gas produced by TiH_2, which counteracts gas losses. Because of these unknown parameters it is difficult to verify the diffusion equation. Nevertheless, the time scale observed in Fig. 7c is in the same order as predicted by Eq. 7.

The thickness *d* has to be small enough for the shaded region in Fig. 12 to feel the influence of the pressure inside the μB. If the μB is far away from the bubble it remains in equilibrium with the surrounding melt since the melt being under1 bar pressure cannot dissolve more hydrogen than the solubility limit permits. Consequently, no concentration gradient is established between the μB and the bubble. As discussed earlier, films (cell walls in the case of solid foam) are thinner than Plateau borders and nodes. Because of this, the average distance between a μB and a bubble is smaller inside films compared to that inside Plateau borders and nodes. Therefore, the μBs inside films shrink or disappear faster than the μBs inside Plateau borders and nodes. In Figs. 8 and 9 only small μBs are found inside cell walls, while Plateau borders contain larger ones.

The above model is valid for the hydrogen μBs that form by the decomposition of TiH_2. When μBs form from the gas produced by the decomposition of adsorbates during the foaming process, the diffusion scenario is different. The adsorbates on the surfaces of aluminium powders used for processing the foamable solid precursors are present in the form of several types of aluminium hydroxides that decompose upon heating during the foaming stage into oxides and water vapour. For example, $Al(OH)_3$ decomposes as follows [35]:

$$2Al(OH)_3 \rightarrow Al_2O_3 + 3H_2O. \quad (8)$$

The water vapour readily reacts with Al

$$2Al + 3H_2O \rightarrow Al_2O_3 + H_2. \quad (9)$$

μBs created by this hydrogen are covered by the oxide that formed through these reactions. The cells/bubbles of the foams produced by pressure-induced foaming (PIF) also form from the same hydrogen [17]. Chethan et al. have shown that in solidified zinc foams made following the PM route the surface of micropores (they called them ‘satellite pores’) is fully covered by oxide

layers [36]. The diffusivity of hydrogen in Al_2O_3 is 3.32×10^{-8} cm^2s^{-1} at 660 °C, which is five orders of magnitude smaller than that in liquid aluminium. For this, the gas loss from such µBs in liquid foam is controlled by the oxide layer which significantly slows down the process and makes these µBs stable for a longer time [33]. Hence, the µBs observed for longer holding time in liquid foams are more likely to be created by the hydrogen produced from adsorbates than from TiH_2.

Coalescence and diffusion are both time dependent and their effect increases with HT [29, 33]. Therefore, microporosity decreases with increasing HT, see Figs. 2 and 5. For AlSi6Cu4 foams, microporosity reduces to a constant level of 3% for 1500 s or longer HT. Interestingly, AlSi6Cu4 without TiH_2 foam also contains 3% microporosity for 1500 s HT. This again implies that a major part of this microporosity is created by the gas produced by adsorbates.

The foaming parameters are identical for AlSi7 and AlSi6Cu4 foams, but due to their different melting range AlSi6Cu4 remained in the liquid state longer than AlSi7. This results in a lower amount of microporosity in AlSi6Cu4 than in AlSi7 for the same HT. AlSi11 foams were held at 30 K above their liquidus temperature, which is higher compared to the superheating for AlSi7 and AlSi6Cu4 foams. Hence, AlSi11 foams were also held in the liquid state for a longer time than AlSi7 and AlSi6Cu4 foams. This led to a lower level of microporosity in AlSi11. On the other hand, even though AlCu13Mg4 has the longest melting range it contains a high level of microporosity (13%). Compared to other alloys, this alloy contains additional gas sources because the AlMg50 intermetallic alloy powder that was used for the processing of this alloy contains a significant amount of hydrogen [28, 37]. Hence, a high level of microporosity is found in this alloy.

4.4. Influence of microporosity on feeding

The solidification mechanism of the metallic component of aluminium foams is different from that in bulk aluminium alloys for two reasons: the small thickness of the metallic component and the presence of µBs prior to solidification. In bulk alloys, µBs form towards the end of solidification,whereas in aluminium foams they are already present when solidification starts as becomes obvious from Figs. 6 and 7 where µBs are present in fully liquid foams. A schematic of the microstructure during the initial stage of solidification in the presence of micropores is shown in Fig. 13. Since it refers to the initial stage of solidification, the micropores shown here are µBs present prior to solidification. Additional micropores will form at some point during solidification. The depiction of dendrites alongside micropores was conceptualized by looking at micrographs, e.g., see Figs. 2–4 and by consulting the review paper published by Lee et al. [38]. Moreover, Campbell suggested that for thin sections, where there are only few grains across the wall section, feeding is more difficult compared to thick sections [2]. This is because grains are restrained by their contact with the wall. This also applies to metal foams since the thicknesses of cell walls or Plateau borders are about 50–200 µm and 100–1000 µm, respectively. This situation is similar to what is depicted in Fig. 13.

The micropores that are present from the beginning of solidification modify melt feeding in two ways. The presence of micropores increases the effective viscosity of the melt similar to solid particles. However, under shear stresses, for instance during feeding, the viscosity decreases more than that of a particle-containing melt because micropores are deformable whereas solid particles are not [39-40]. Secondly, micropores are trapped in between growing dendrites and make feeding more difficult [41]. For this, in metal foams feeding stops at an early stage compared to the solidification of bulk alloys. Consequently, the amount of shrinkage

microporosity is higher in metal foams compared to that in bulk alloys. A micropore trapped in the junction of dendrites can result in a large irregular micropore by merging with shrinkage microporosity [41-42], similar to what is shown in the inset of Fig. 2a. With increasing HT, as micropores shrink/disappear as shown in Fig. 7, the number of such irregular micropores decreases.

4.5. Influence of micropores on structure of solidified foam

During solidification of aluminium foams, *solidification expansion* generates defects, mostly broken cell walls [43]. The same defects may also form under the influence of microporosity. In comparison to TiH_2-containing foams (Fig. 2), in TiH_2-free foams the thickness of cell walls is small as seen in Figs. 3a and 3b. For instance, the micropore shown in the inset of Fig. 3c is separated by cells 1 and 2 by 15-µm to 20-µm thick cell walls. During solidification of these very thin cell walls feeding is largely inhibited thus causing these very thin parts of the cell wall to rupture. If this rupture takes place towards the end of solidification it cannot lead to the coalescence of the two adjacent cells (cell 1 and 2) and consequently the cell wall is only partially broken [43]. As a result, the cell wall that contained this micropore appears broken in the solidified structure as some of them are seen in Fig. 3c. On the other hand, as the number of micropores decreases with increasing HT, such defects also diminish, see Fig. 3d.

In TiH_2-containg foams, cell walls are thicker(compare Figs. 2 and 3) and therefore the number and extent of such defects is small. Nevertheless, in some cases such defects were observed. For instance, in Fig. 14, the part of the cell walls separating a micropore from the adjacent cells breaks, creating a connection between the two cells.

Based on above results it can be stated that micropores can influence the cellular structure of metal foams by creating interconnections among cells. Solórzano et al. have shown that

apparently closed cell metal foams such as Alporas and Alulight foams have actually interconnected cells [44]. The partially broken cell walls caused by the presence of micropores could contribute towards such interconnections. Such interconnections/defects could be beneficial in terms of fluid transport or sound attenuation, but they might be detrimental in terms of mechanical properties as for bulk alloys.

Because of the absence of shrinkage microporosity in AlSi6Cu4 without TiH_2 and AlCu13Mg4 foams, most of the micropores are near-spherical as seen in Figs. 8 and 10. In AlSi6Cu4 foams, shrinkage micropores enhance the formation of large irregular micropores by merging with gas micropores as mentioned earlier.

4.6. *Controlling microporosity*

The present study shows that microporosity can be reduced by increasing HT or by choosing the right alloy composition. Beside this, avoiding the use of a blowing agent may also be considered in order to achieve a defect-free structure. Our previous study demonstrated that an increase in cooling rate reduces the size of both shrinkage and gas micropores [13]. Powder compaction under vacuum atmosphere led to an improved structure of foams compared to the foams produced from powder compacts that are processed under air [45].

5. Conclusions

- Aluminium foams contain micropores that are caused either by the individual or by the combined effect of gas precipitation and foam shrinkage. While in bulk alloys the source of gas is hydrogen that precipitates during solidification, aluminium foams contain additional sources, namely the hydrogen produced by the blowing agent TiH_2 and the decomposition products of adsorbates introduced by the metal powder.

- Unlike in bulk alloys, micropores are present even before solidification starts in aluminium foams.
- The gas produced by the adsorbates contributes a major part to the microporosity formed in the liquid state especially when the holding time (HT) is short.
- The amount of microporosity in TiH_2-containing and TiH_2-free foams is the same, and its amount decreases with increasing HT.
- While foams of the short-freezing range alloy foams such as pure aluminium and AlSi11 show low levels of microporosity, the level is much higher in the long-freezingrange alloy foams.
- Micropores found inside cell walls are smaller than those found inside Plateau borders and nodes.
- For shorter HT, when the level of micropores is high, feeding is restricted leading to the formation of large irregular micropores. Micropores promote generation of macrostructural defects such as broken cell walls and cell interconnections.

Acknowledgements

The authors would like to thank H. Kropf for preparation of metallographic samples and A. Hilger for helping with X-ray tomography measurements. The first author would like to thank K.C. Hari Kumar for doing the liquid fraction calculation.

Appendix

Calculation of concentration difference

According to the Sievert's law the solubility of hydrogen in liquid aluminium is proportional to the square root of the pressure. If S_H is the solubility of hydrogen in liquid aluminium at

atmospheric pressure P_{atm} , which is 1 bar, and $S_{H(P)}$ is the solubility at a pressure P then we can write

$$\frac{S_H}{S_{H(P)}} = \sqrt{\frac{P_{\text{atm}}}{P}} \qquad \text{(A1)}$$

or $S_{H(P)} = S_H \times \sqrt{\frac{P}{P_{\text{atm}}}}$. (A2)

The pressure inside a bubble P_{B} of radius R is

$$P_B = P_{\text{atm}} + \frac{2\gamma}{R} \qquad \text{(A3)}$$

and the pressure inside a microbubble $P_{\mu\text{B}}$ of radius r is

$$P_{\mu B} = P_{\text{atm}} + \frac{2\gamma}{r}. \qquad \text{(A4)}$$

Therefore, according to Eq. A2, the solubility of hydrogen at the Al-B interface is

$$S_{Al-B} = \frac{S_H}{\sqrt{P_{\text{atm}}}}\sqrt{P_{\text{atm}} + \frac{2\gamma}{R}} \qquad \text{(A5)}$$

and the solubility of hydrogen at the Al-μB interface is

$$S_{Al-\mu B} = \frac{S_H}{\sqrt{P_{\text{atm}}}}\sqrt{P_{\text{atm}} + \frac{2\gamma}{r}} \quad . \qquad \text{(A6)}$$

Under equilibrium conditions, the concentration of hydrogen at the respective interface is equal to its solubility limit [33]. Therefore, the concentration difference ΔC (C = concentration) between the two interfaces can be expressed as follows.

$$\Delta C = C_{Al-\mu B} - C_{Al-B} = \frac{S_H}{\sqrt{P_{\text{atm}}}}\left(\sqrt{P_{\text{atm}} + \frac{2\gamma}{r}} - \sqrt{P_{\text{atm}} + \frac{2\gamma}{R}}\right) \qquad \text{(A7)}$$

Table 1: Alloy compositions and foaming parameters. The average cooling rate in all cases was 1 K/s.

composition (wt.%)	TiH_2 used?	holding times (s)	foaming (interior) temperature (°C)	pressure profile
Al	yes	50	670	constant at 1 bar
AlSi7	yes	200	620	constant at 1 bar
AlSi11	yes	200	620	constant at 1 bar
AlSi6Cu4	yes	200, 600, 1000, 1500, 2500	620	constant at 1 bar
AlSi6Cu4	no	200, 1500	620	5 bar during melting, then reduced to 1 bar
AlCu13Mg4	no	200	620	5 bar during melting, then reduced to 1 bar

Table 2: Solidification shrinkage, effective volume of hydrogen precipitation (prec.) and solubility (sol.) in Al/Al-alloys assuming hydrogen saturation in the melt. The volumes given are at the precipitation temperatures and at 700 °C. (T_L: liquidus temperature)

alloy	melting point/range, (°C)	solidification shrinkage (vol.%)	total H_2 prec. at T_L (vol.%) [15, 46]	H_2 sol. at 700 °C (vol.%) [24-25]
Al	660	7 from Ref. [2]	5	8
AlSi7	577–617	6 from Ref. [26]	3.05	6.13
AlSi11	577–590	5 from Ref. [27]	1.86	5.5
AlSi6Cu4	519–611	6 from Ref. [26]	2.5	4.9
AlCu13Mg4	503–604	notknown	3.8 (estimated)	7.6

Melting range for AlSi7, AlSi6Cu4 and AlCu13Mg4 was extracted from the graphs in Fig. 11.

References

[1] C.H. Cáceres, B.I. Selling, Casting defects and the tensile properties of an AlSiMg alloy, Mat. Sci. Eng. A 220 (1996) 109-116.

[2] J. Campbell, Castings: The New Metallurgy of Cast Metals, second ed., Butterworth-Heinemann, Oxford, United Kingdom, 2003.

[3] M.J. Couper, A.E. Neeson, J.R. Griffiths, Casting defects and the fatigue behaviour of an aluminium casting alloys, Fatigue Frac. Eng. Mater.Struct. 13 (1990) 213-227.

[4] C.D. Lee, Effects of microporosity on tensile properties of A356 aluminum alloy, Mat. Sci. Eng., A 464 (2007) 249-254.

[5] E. Andrews, W. Sanders, L.J. Gibson, Compressive and tensile behaviour of aluminum foams, Mat. Sci. Eng., A 270 (1999) 113-124.

[6] I. Jeon, T. Asahina, The effect of structural defects on the compressive behavior of closed-cell Al foam, Acta Mater. 53 (2005) 3415-3423.

[7] Y. Sugimura, J. Meyer, M. He, H. Bart-Smith, J. Grenstedt, A. Evans, On the mechanical performance of closed cell Al alloy foams, Acta Mater. 45 (1997) 5245-5259.

[8] L. Gibson, M. Ashby, Cellular solids: structure and properties, Cambridge Univ Press, 1999.

[9] H. Toda, M. Takata, T. Ohgaki, M. Kobayashi, T. Kobayashi, K. Uesugi, K. Makii, Y. Aruga, 3-D image-based mechanical simulation of aluminium foams: effects of internal microstructure, Adv. Eng. Mater. 8 (2006) 459-467.

[10] A. Gokhale, G. Patel, Origins of variability in the fracture-related mechanical properties of a tilt-pour-permanent-mold cast Al-alloy, Scr. Mater. 52 (2005) 237-241.

[11] T. Ohgaki, H. Toda, M. Kobayashi, K. Uesugi, M. Niinomi, T. Akahori, T. Kobayash, K. Makii, Y. Aruga, In situ observations of compressive behaviour of aluminium foams by local tomography using high-resolution X-rays, Phil. Mag. 86 (2006) 4417-4438.

[12] H. Toda, T. Kobayashi, M. Niinomi, T. Ohgaki, M. Kobayashi, N. Kuroda, T. Akahori, K. Uesugi, K. Makii, Y. Aruga, Quantitative assessment of microstructure and its effects on compression behavior of aluminum foams via high-resolution synchrotron X-ray tomography, Metall. Mater. Trans. A 37 (2006) 1211-1219.

[13] M. Mukherjee, U. Ramamurty, F. Garcia-Moreno, J. Banhart, The effect of cooling rate on the structure and properties of closed-cell aluminium foams, Acta Mater. 58 (2010) 5031-5042.

[14] F. Garcia-Moreno, N. Babcsan, J. Banhart, X-ray radioscopy of liquid metal foams: influence of heating profile, atmosphere and pressure, Coll. Surf. A 263 (2005) 290-294.

[15] M. Mukherjee, F. Garcia-Moreno, J. Banhart, Solidification of metal foams, Acta Mater. 58 (2010) 6358-6370.

[16] F. Garcia-Moreno, J. Banhart, Foaming of blowing agent-free aluminium powder compacts, Coll. Surf. A 309 (2007) 264-269.

[17] F. García-Moreno, M. Mukherjee, C. Jiménez, J. Banhart, Pressure-induced foaming of metals, JOM 67 (2015) 955-965.

[18] F. Garcia-Moreno, A. Rack, L. Helfen, T. Baumbach, S. Zabler, N. Babcsan, J. Banhart, T. Martin, C. Ponchut, M. Di Michiel, Fast processes in liquid metal foams investigated by high-speed synchrotron x-ray microradioscopy, Appl. Phy. Lett. 92 (2008) 134104-134101-134103.

[19] A. Rack, F. García-Moreno, L. Helfen, M. Mukherjee, C. Jiménez, T. Rack, P. Cloetens, J. Banhart, Hierarchical radioscopy using polychromatic and partially coherent hard synchrotron radiation, Appl. Opt. 52 (2013) 8122-8127.

[20] C. Jiménez, F. Garcia-Moreno, M. Mukherjee, O. Goerke, J. Banhart, Improvement of aluminium foaming by powder consolidation under vacuum, Scr. Mater. 61 (2009) 552-555.

[21] J. Anson, J. Gruzleski, The quantitative discrimination between shrinkage and gas microporosity in cast aluminum alloys using spatial data analysis, Mater. Charact. 43 (1999) 319-335.

[22] B. Sundman, B. Jansson, J.-O. Andersson, The thermo-calc databank system, Calphad 9 (1985) 153-190.

[23] I. Ansara, A. Dinsdale, M. Rand, COST 507 Definition of thermochemical and thermophysical properties to provide a database for the development of new light alloys: thermochemical database for light metal alloys, Office for Official Publications of the European Communities, 1998.

[24] P.N. Anyalebechi, Analysis of the effects of alloying elements on hydrogen solubility in liquid aluminum alloys, Scr. Metall. Mater. 33 (1995) 1209-1216.

[25] P.N. Anyalebechi, Attempt to predict hydrogen solubility limits in liquid multicomponent aluminum alloys, Scr. Mater. 34 (1996) 513-517.

[26] Thermotech Ltd, JMatPro: Materials property simulation package, United Kingdom. <http://www.thermotech.co.uk/>.

[27] T. Magnusson, L. Arnberg, Density and solidification shrinkage of hypoeutectic aluminum-silicon alloys, Metall. Mater. Trans. A 32 (2001) 2605-2613.

[28] M. Mukherjee, F. Garcia-Moreno, C. Jiménez, J. Banhart, Al and Zn foams blown by an intrinsic gas source, Adv. Eng. Mater. 12 (2010) 472-477.

[29] F. Garcia-Moreno, E. Solorzano, J. Banhart, Kinetics of coalescence in liquid aluminium foams, Soft Matter 7 (2011) 9216-9223.

[30] C. Garcia-Cordovilla, E. Louis, A. Pamies, The surface tension of liquid pure aluminium and aluminium-magnesium alloy, J. Mater. Sci. 21 (1986) 2787-2792.

[31] J. Goicoechea, C. Garcia-Cordovilla, E. Louis, A. Pamies, Surface tension of binary and ternary aluminium alloys of the systems Al-Si-Mg and Al-Zn-Mg, J. Mater. Sci. 27 (1992) 5247-5252.

[32] B. Keene, Review of data for the surface tension of pure metals, Int. Mater. Rev. 38 (1993) 157-192.

[33] M. Mukherjee, F. Garcia-Moreno, J. Banhart, Collapse of aluminum foam in two different atmospheres, Metall. Mater. Trans. B 41 (2010) 500-504.

[34] W. Eichenauer, J. Markopoulos, Messung des Diffusionskoeffizienten von Wasserstoff in flüssigem Aluminium, Z. Metallkd. 65 (1974) 649-652.

[35] K. Wefers, C. Misra, Oxides and hydroxides of aluminum, Alcoa Technical Paper No. 19, Revised, Alcoa Laboratories, Alcoa Center, PA, 1987, 1987.

[36] A. Chethan, F. Garcia-Moreno, N. Wanderka, B. Murty, J. Banhart, Influence of oxides on the stability of zinc foam, J. Mater. Sci. 46 (2011) 7806-7814.

[37] C. Jiménez, F. Garcia-Moreno, J. Banhart, G. Zehl, Effect of relative humidity on pressure-induced foaming (PIF) of aluminium-based precursors. in: L.P. Lefebvre, J. Banhart, D. Dunand (Eds.), Proceedings of Porous Metals and Metallic foams, Montreal, Canada.: DEStech Publications, 2007. pp.59-62.

[38] P.D. Lee, A. Chirazi, D. See, Modeling microporosity in aluminum–silicon alloys: a review, J. Light Met. 1 (2001) 15-30.

[39] M. Manga, M. Loewenberg, Viscosity of magmas containing highly deformable bubbles, J. Volcanol. Geotherm. Res. 105 (2001) 19-24.

[40] A.C. Rust, M. Manga, Effects of bubble deformation on the viscosity of dilute suspensions, J. Non-Newtonian Fluid Mech. 104 (2002) 53-63.

[41] D.M. Stefanescu, Science and engineering of casting solidification, second ed., Springer, New York, 2009.

[42] A.S. Sabau, S. Viswanathan, Microporosity prediction in aluminum alloy castings, Metall. Mater. Trans. B 33 (2002) 243-255.

[43] M. Mukherjee, F. Garcia-Moreno, J. Banhart, Defect generation during solidification of aluminium foams, Scr. Mater. 63 (2010) 235-238.

[44] E. Solórzano, M.A. Rodríguez-Pérez, J.A. de Saja, Do we really produce closed cell metallic foams, in: J. Hirsch, B. Skrotzki, G. Gottstein (Eds.), Aluminum Alloys: Their Physical and Mechanical Properties, vol. Vol-2: Wiley-VCH, Weinheim, 2008. pp.2200-2206.

[45] C.E. Jiménez, Characterization and modification of powders used to make aluminium-based metal foams. Technische Universität Berlin, 2009.

[46] P. Lutze, J. Ruge, Wasserstoff in Aluminium und seine Legierungen, Metall 8 (1990) 741-748.

Figures

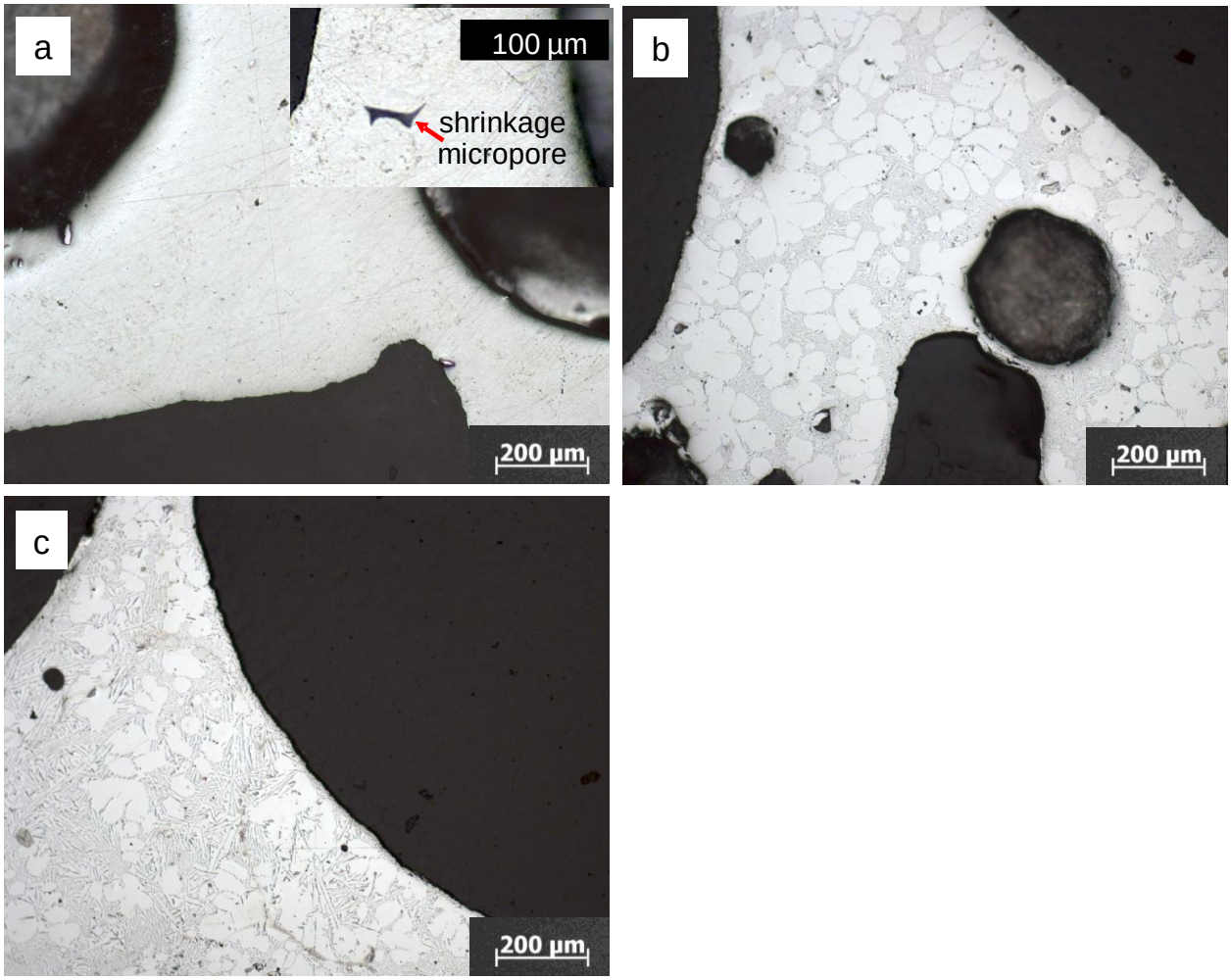

Figure 1: Microstructure of (a) pure Al, (b) AlSi7 and (c) AlSi11 foams. Inset in (a) shows shrinkage micropore in another region of the same sample. The holding times for (a), (b) and (c) are 50, 200 and 200 s, respectively.

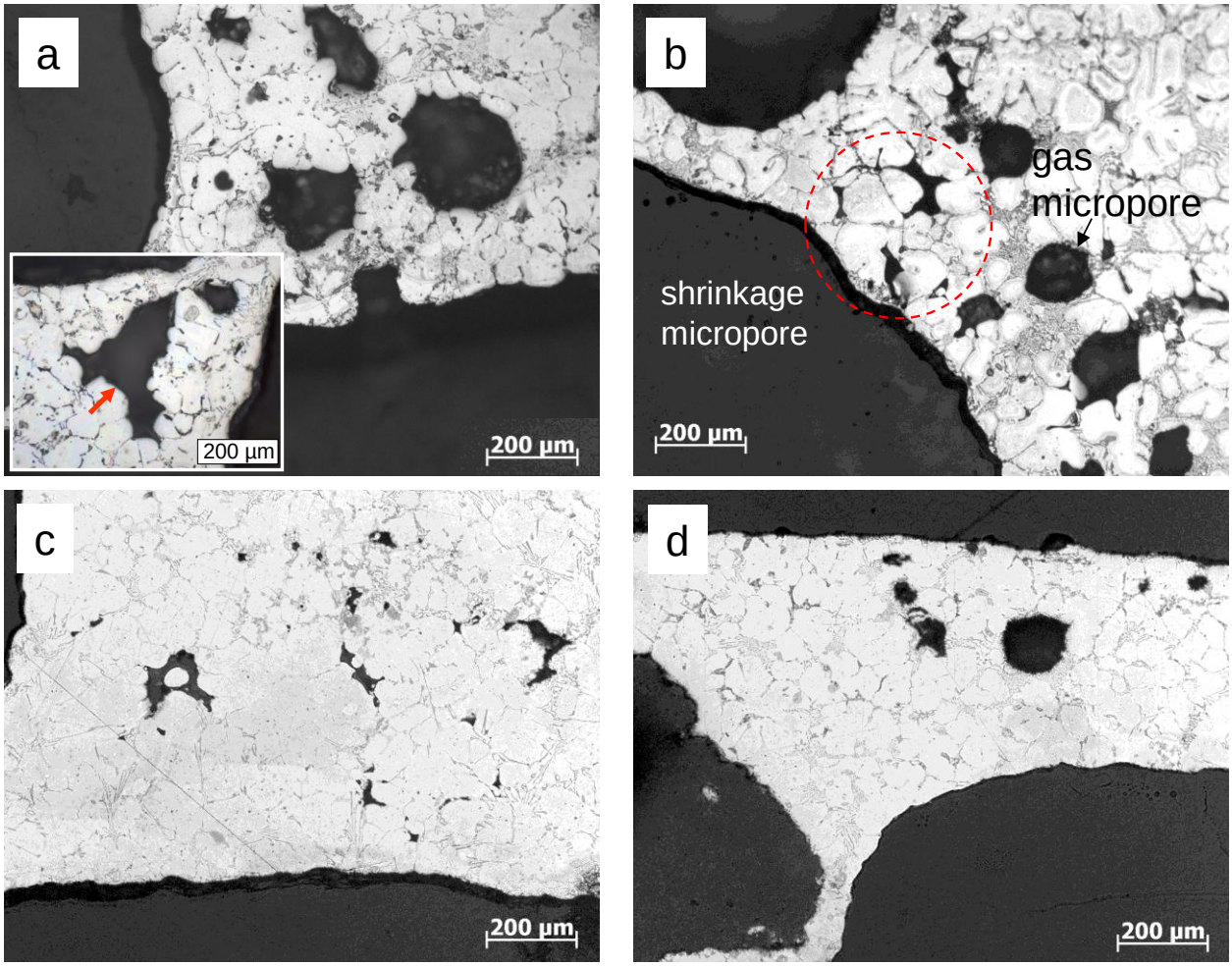

Figure 2: Microstructures of AlSi6Cu4 foams. The holding times are (a) 200 s, (b) 600 s, (c) 1000 s, (d) 2500 s. Inset of Fig. 2a: An arrow indicates a micropore in the cell wall of a AlSi6Cu4 (200 s HT) foam.

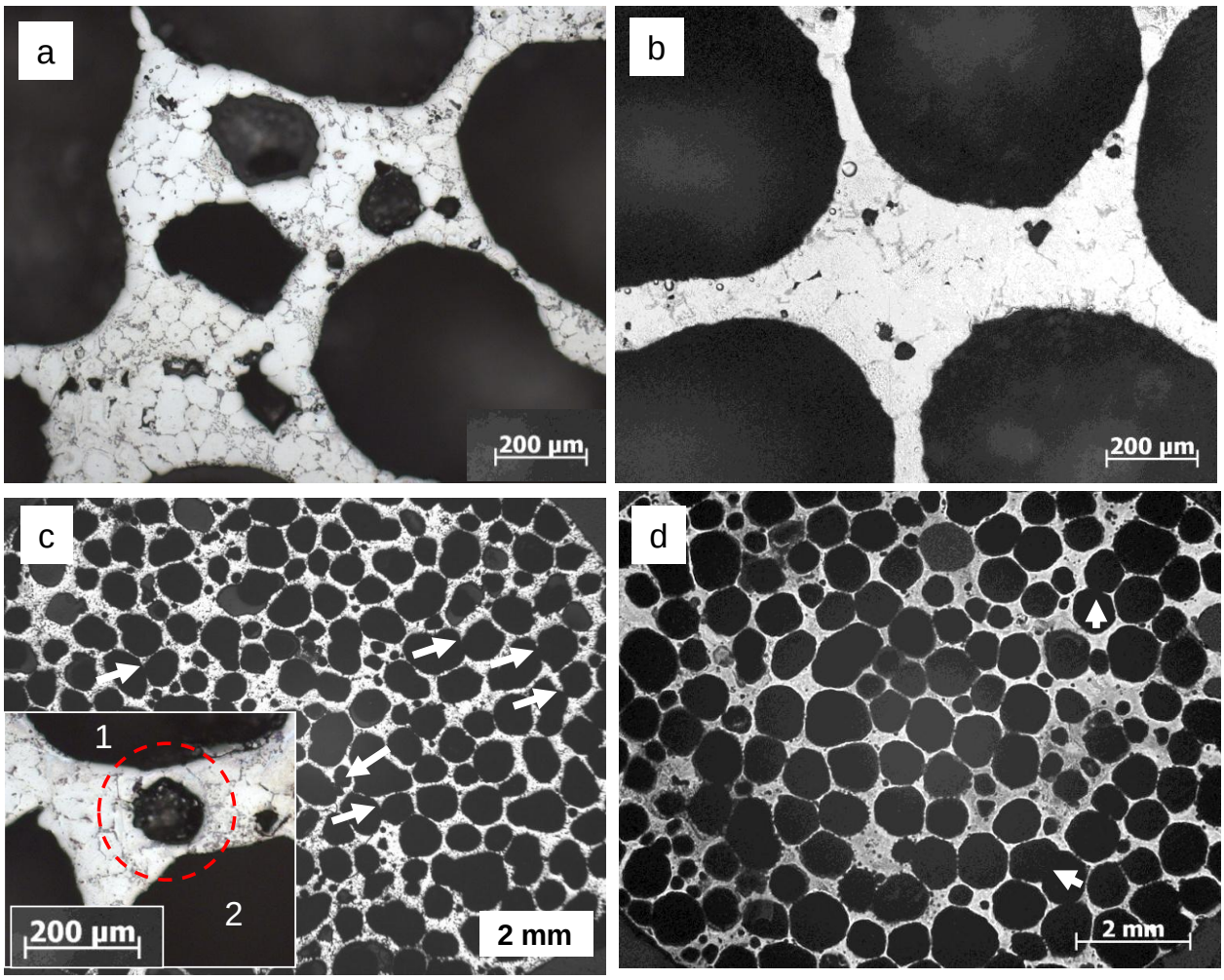

Figure 3: Micro- and macrostructure of AlSi6Cu4 foamed without TiH_2. The holding times for (a) and (c) are 200 s, and for (b) and (d) 1500 s. The arrows in (c) and (d) indicate broken cell walls. The inset in Fig. 3c shows a micropore (marked by dashed circle).

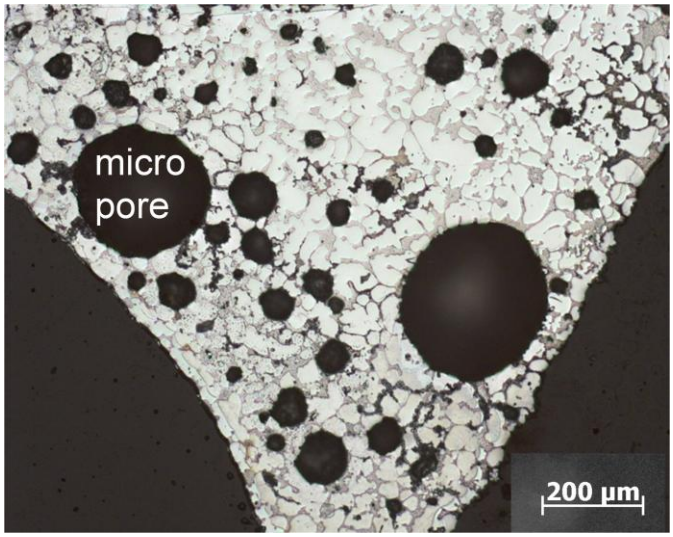

Figure 4: Microstructure of AlCu13Mg4 foam.

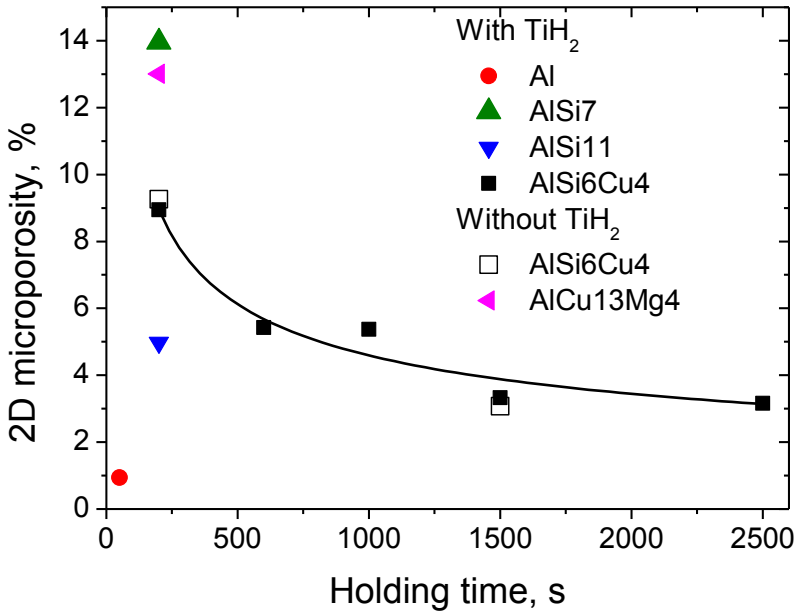

Figure 5: 2D microporosity for different holding times. The solid line is the fit of the data for AlSi6Cu4 (foamed with TiH_2).

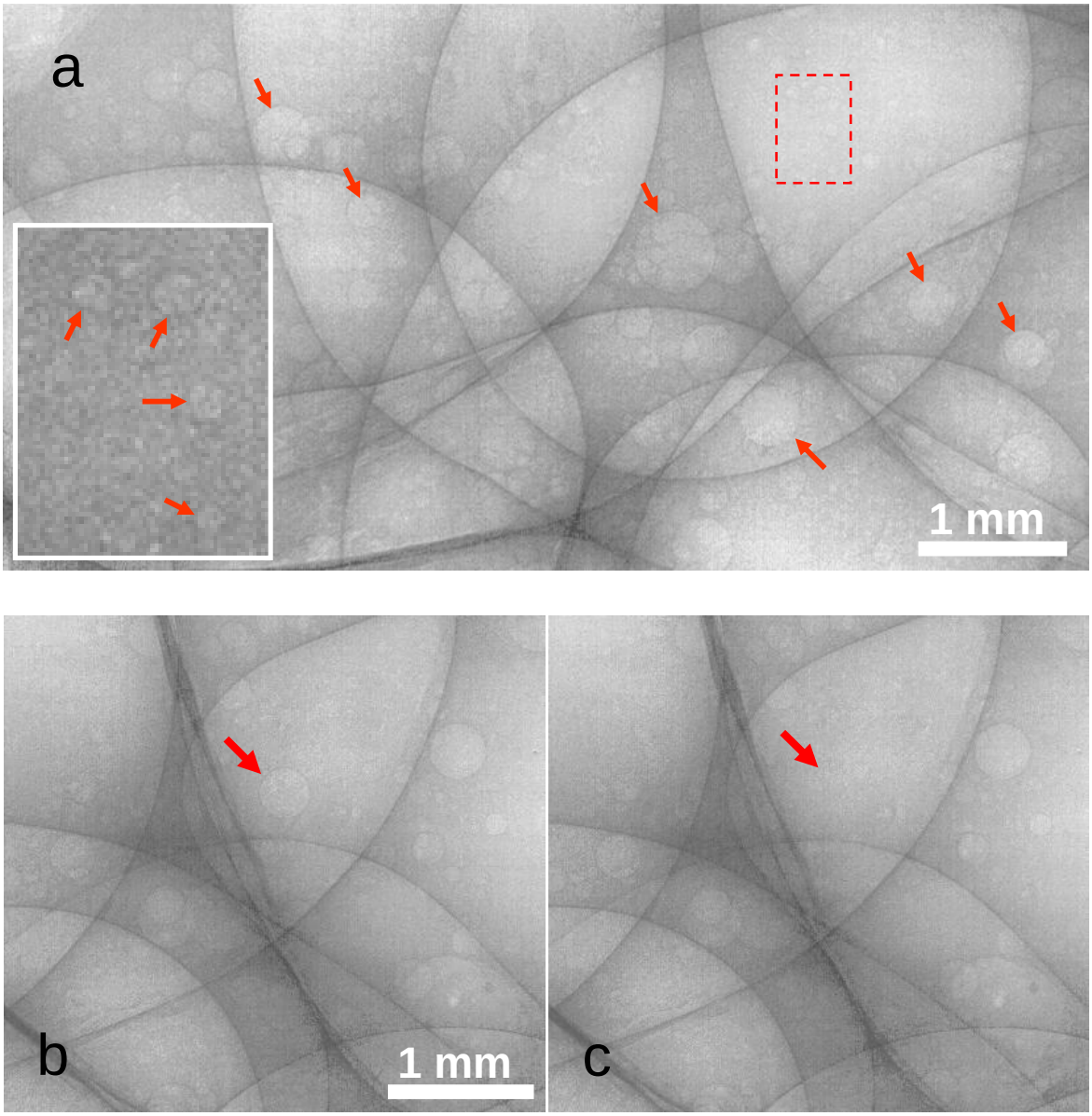

Figure 6: (a-c) Radiograph of AlSi6Cu4 foam in the liquid state imaged by synchrotron X-ray radioscopy. Microbubbles are seen as small circular objects, some of which are indicated by arrows. Inset of Fig. 6a: Enlarged and contrast-modified view of the region in (a) defined by broken rectangle. The microbubbles marked by arrows in the inset are present in the flat part of a cell wall and range between 50 µm and 100 µm in diameter. The width of the inset is 500 µm. The microbubble indicated by an arrow in (b) disappears 800 µs later in (c).

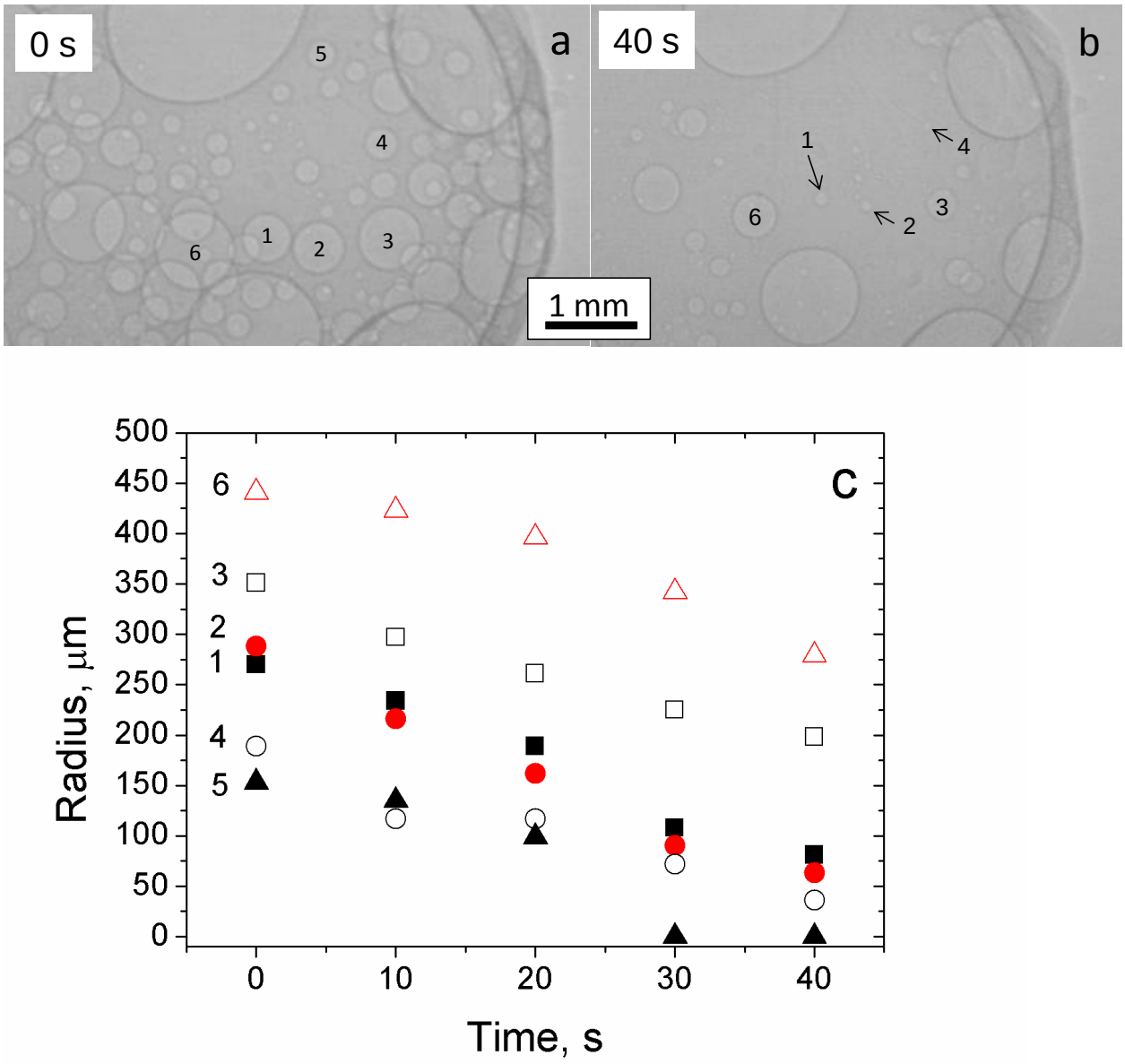

Figure 7: (a-b) Radiograph of Al foam in the liquid state imaged by synchrotron X-ray radioscopy. In (a) six microbubbles are marked by numbers 1–6. The evolution of these microbubbles is presented in terms of radius vs. time in (c). The numbers beside each type of symbol in (c) indicate a microbubble in (a) with the same number. The radiograph in (a) and (b) correspond to the 0 s and 40 s stage of (c), respectively.

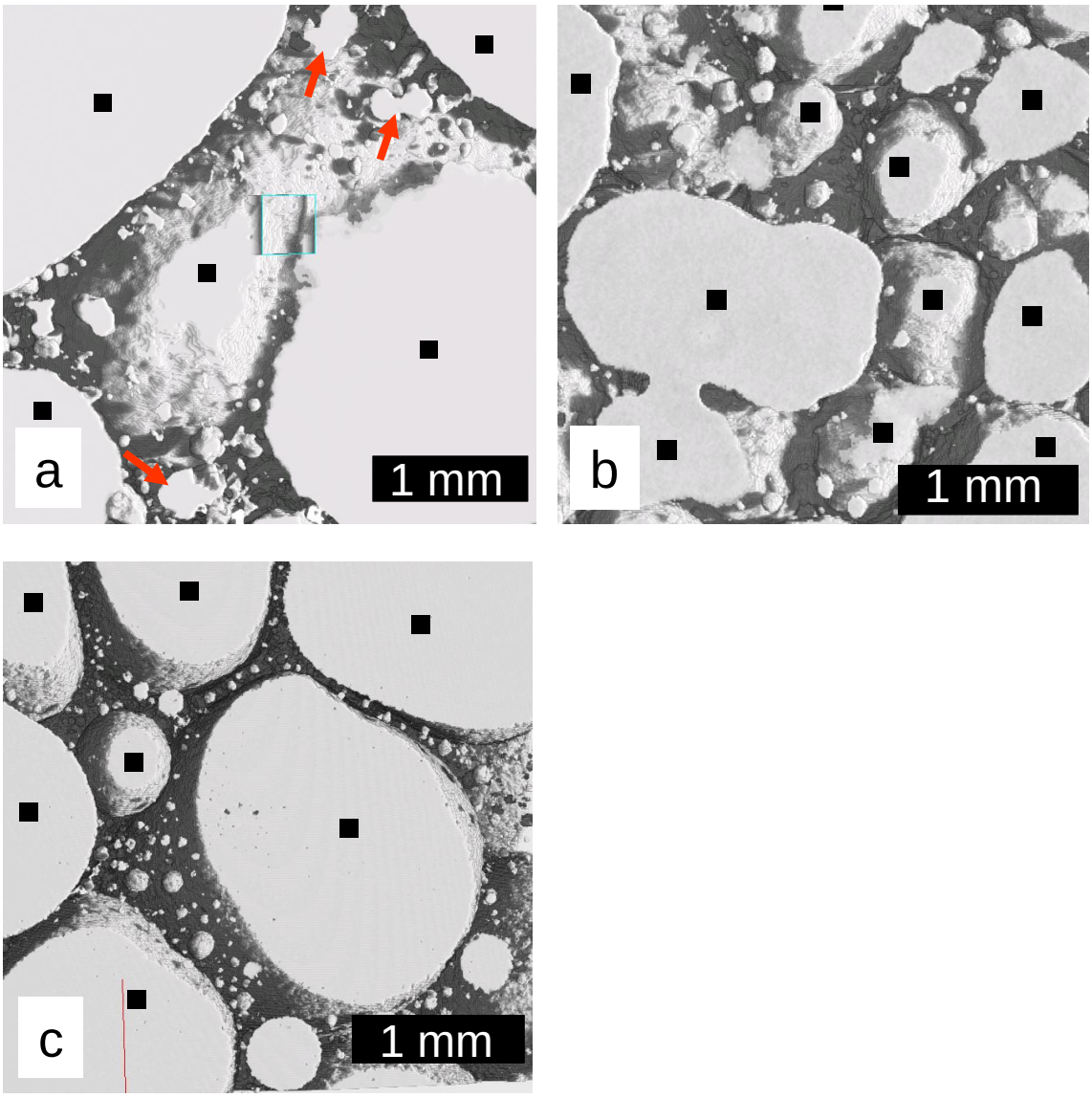

Figure 8: 3D X-ray tomographic reconstruction of solid foam where only cells and micropores are shown as white objects and the metal is made transparent. These images were obtained by rendering 3D datasets and illuminating the 3D volume with a light source from the right. This light source produces shadows which appears dark and improve visibility of features. (a) AlSi6Cu4 foam, (b) AlSi6Cu4 foamed without TiH_2 and (c) AlCu13Mg4 foam. All samples were foamed with 200 s HT. Cells are marked by solid squares. The micropores are seen as small objects between cells. Arrows in (a) indicate elongated pores.

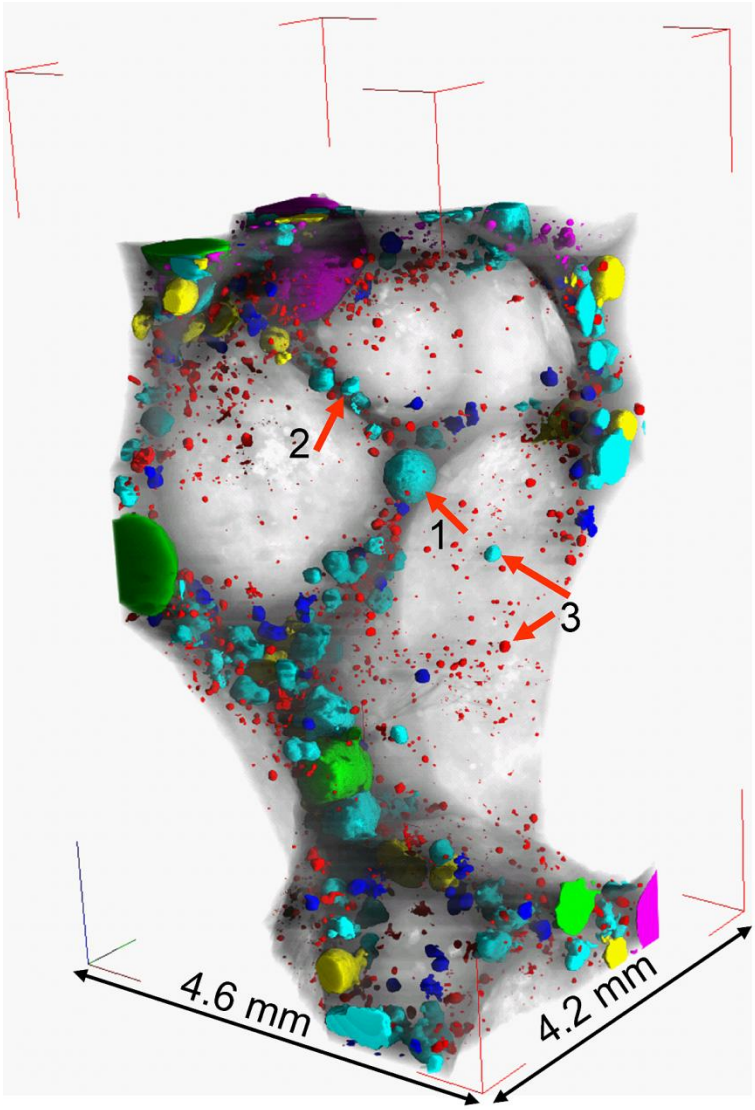

Figure 9: 3D visualization obtained by X-ray tomography of the arrangement of micropores (coloured objects) in solid AlSi6Cu4 foam (200 s HT). Cells are omitted from this volume, and metallic matrix is made partially transparent. Micropore(s) inside nodes, a Plateau border and a cell wall are indicated by arrows numbered 1, 2 and 3, respectively. The colours of the micropores merely help to distinguish different micropores.

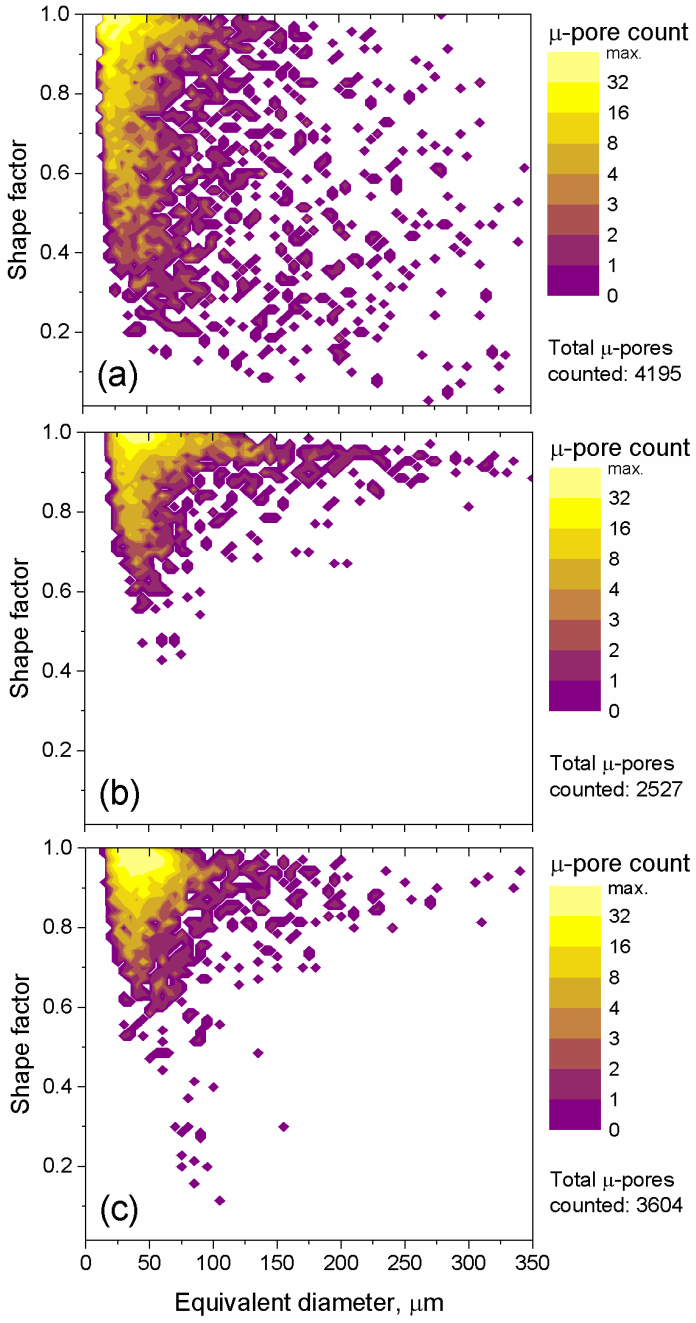

Figure 10: Micropore count (colour-scale) for the foams shown in Fig. 8 vs. shape factor and equivalent diameter for (a) AlSi6Cu4, (b) AlSi6Cu4 without TiH_2 and (c) AlCu13Mg4 alloys, all foamed with 200 s HT. Both analysed ranges 0–350 μm for equivalent diameter and 0–1 for shape factor were divided into 70 intervals. Total micropores counted are also indicated.

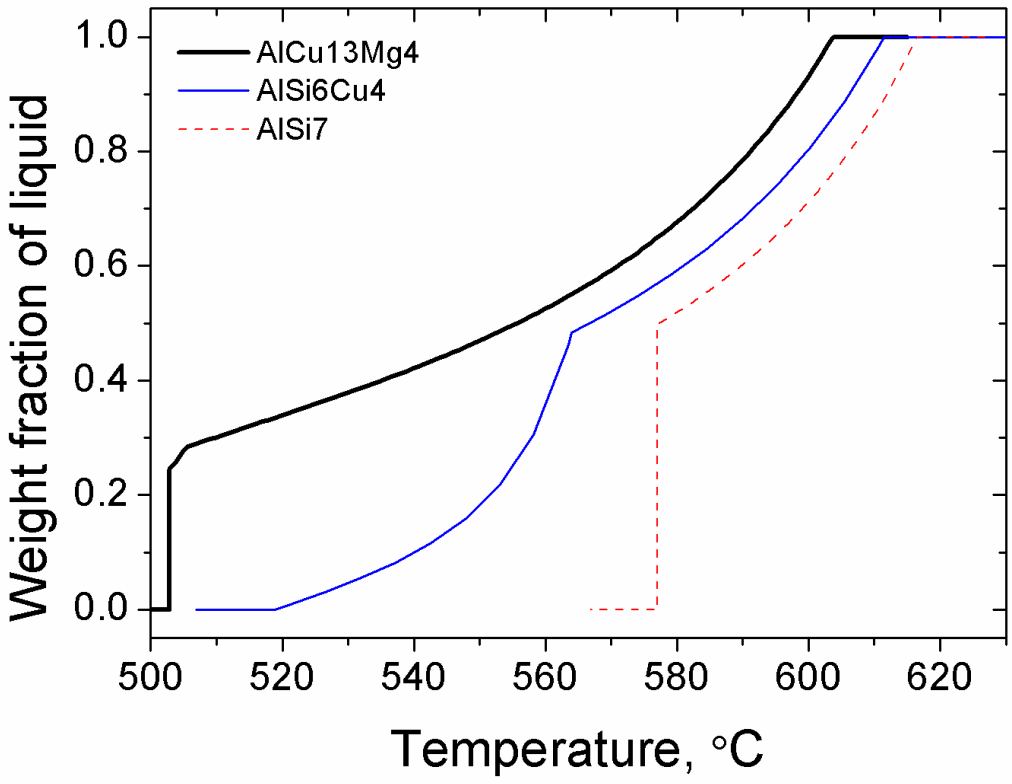

Figure 11: Liquid fraction as a function of temperature during the solidification of AlSi7, AlSi6Cu4 and AlCu13Mg4 alloys.

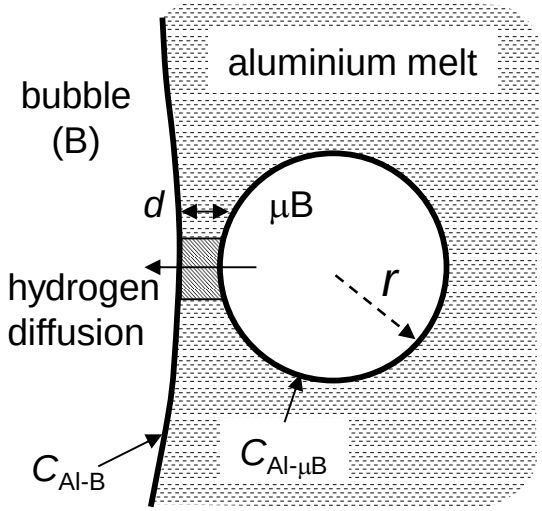

Figure 12: Schematic of hydrogen diffusion from a microbubble (μB) to a bubble (B) in aluminium foam. *r* is the radius of the μB, *d* is the minimum distance between the μB and the bubble. It is assumed that diffusion takes place only through the shaded region which in 3D covers 10% of the μB surface. $C_{Al-\mu B}$ and C_{Al-B} represent the concentration of hydrogen at the gas-melt interface of the μB and bubble, respectively.

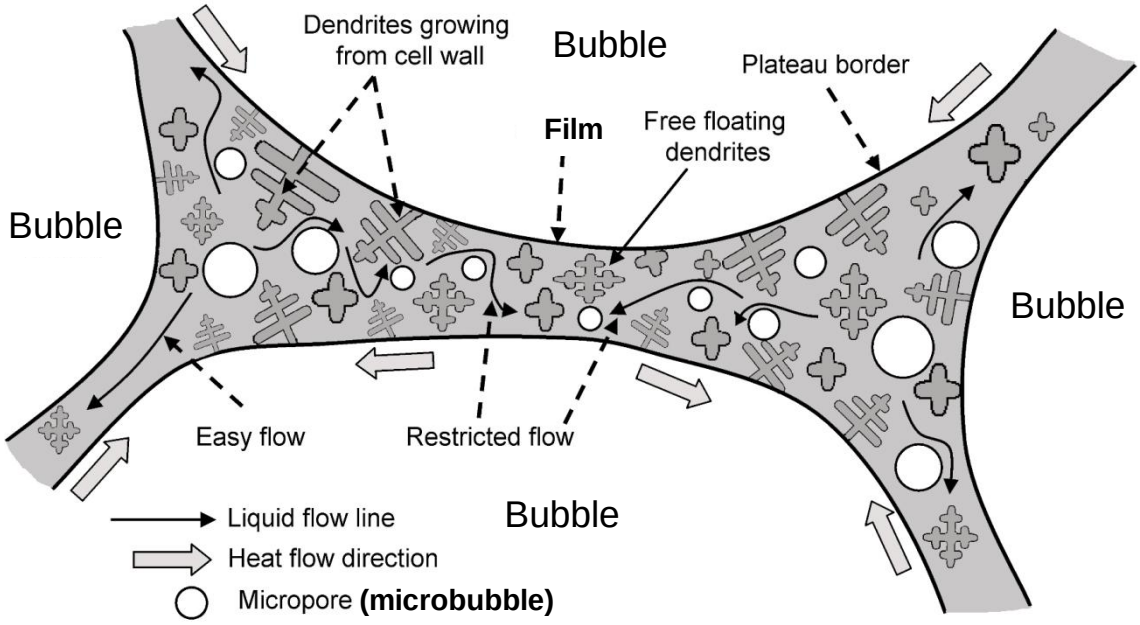

Figure 13: Sketch of the solidification shrinkage-induced liquid flow inside films and Plateau borders in the semi-solid state in the presence of micropores (microbubbles).

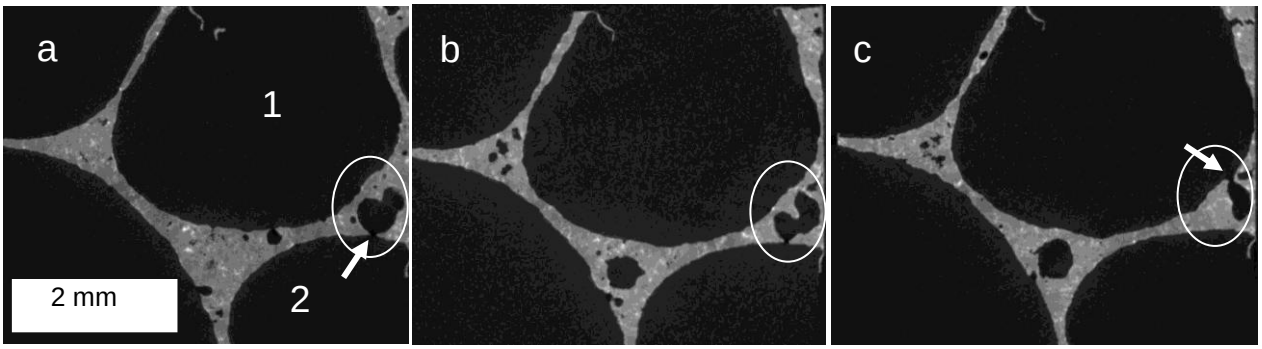

Figure 14: 2D X-ray tomographic sections of cell wall in solid AlSi6Cu4 (200 s HT) foam at three different depths with respect to the direction perpendicular to the image plane. Interconnection of two cells (1 and 2) through a micropore (marked by ellipse) is shown. The connecting points are indicated by arrows. The distance between the sections in (a) and (b) is ~107 µm, in (b) and (c) ~72 µm.

Supplementary Materials

Click here to download Supplementary Material: Mukherjee-Supplementary-materials.docx

*Graphical Abstract

3D visualization obtained by X-ray tomography of the arrangement of micropores (coloured objects) in solid AlSi6Cu4 foam